TRANSACTIONS ON ELECTRICAL AND ELECTRONIC ENGINEERING
IEEJ Trans 2009; **4**: 497–503
Published online in Wiley InterScience (www.interscience.wiley.com). DOI:10.1002/tee.20435

Paper

Metal Vapor Behavior in GTA Welding of a Stainless Steel Considering the Marangoni Effect

Kentaro Yamamoto*[a], Non-member
Manabu Tanaka*, Member
Shinichi Tashiro*, Member
Kazuhiro Nakata*, Non-member
Anthony B. Murphy**, Non-member

A gas tungsten arc in helium was modeled taking into account the contamination of the plasma by metal vapor from the weld pool. The whole region of gas tungsten arc atmosphere including the tungsten cathode, arc plasma and weld pool was treated using a unified numerical model. The anode was of a low sulfur stainless steel or a high sulfur stainless steel. A viscosity approximation was used to express the diffusion coefficient in terms of viscosity of shielding gas and metal vapor. The transient two-dimensional distributions of the temperature, velocity of plasma flow and iron vapor concentration were predicted, together with the weld penetration at the atmospheric pressure. The distribution of the iron vapor is obviously different between the case of a low sulfur stainless steel anode and the case of a high sulfur stainless steel anode. © 2009 Institute of Electrical Engineers of Japan. Published by John Wiley & Sons, Inc.

Keywords: arc, welding, stainless steel, metal vapor, marangoni effect, numerical simulation

Received 8 December 2008; Revised 18 March 2009

1. Introduction

During arc welding, four states of matter including solid, liquid, gas and plasma, simultaneously exist and mutually interact within a volume of only 1000 mm^3. The temperature ranges widely between 20 000 K in the arc plasma, 3000 K in the tungsten cathode, 2000 K in the molten steel, and the room temperature in the surroundings [1]. It has become possible to understand the phenomena in arc welding processes quantitatively due to a recent remarkable progress in computer simulations and observation techniques [2,3]. For example, the authors have developed numerical simulations that calculate the properties of the tungsten cathode, the arc plasma and the weld pool. These simulations have enabled us to visually observe a relationship between the formation of a weld pool and the balance of energy and momentum in each state of matter [4]. However, it has not been possible yet to accurately predict the welding parameters, such as the arc voltage and the weld geometry. For a full understanding and precise prediction of these parameters, it is necessary to understand the behavior of metal vapor in the arc plasma.

Metal atoms generally have more states of low-energy excitation and more likely to be ionized than atoms of shielding gases such as argon and helium. These characteristics contribute to an increase in the radiative emission coefficient and electric conductivity of plasma. It is estimated that the former affects the thermal pinch effect and electric conductivity of plasma, and that the latter does the current density distribution. Tashiro *et al*. [5] conducted a virtual experiment by numerically simulating a pure helium arc and an arc in helium uniformly mixed with 30 mol% iron atoms, and showed that an obvious arc constriction occurred in the latter case. They further reported that the energy efficiency greatly decreased approximately from 80 to 35%. These results suggest that the existence of metal vapor changes the heat source property in arc welding processes and consequently changes the size and the shape of a molten pool.

As noted above, there have been significant advances in the simulation of arc welding. For example, a numerical simulation of the formation of droplets from a steel wire electrode in gas metal arc welding has been reported [6]. However, this simulation is for the pure argon gas shielding and the effect of metal vapor is not considered. Meanwhile, calculations of the behavior of metal vapor in atmospheric plasma have been also reported [7]. However, the conditions in these calculations are far from those in actual welding because a solid electrode with the constant temperature is assumed. It is important for accurate understanding of the arc welding process to consider the mixing of the metal vapor in a model that takes into account the tungsten cathode, the arc plasma and the weld pool.

In the present paper, the authors use a numerical model of stationary GTA welding taking into account the iron vapor

[a] Correspondence to: Kentaro Yamamoto.
E-mail: k-yama@jwri.osaka-u.ac.jp
* Joining and Welding Research Institute, Osaka University 11-1, Mihogaoka, Ibaraki,Osaka 567-0047, Japan
** CSIRO Materials Science and Engineering, PO Box 218, Lindfield NSW 2070, Australia

produced from the weld pool surface, and simulate transient changes in the distribution of the metal vapor, the plasma temperature and the formation of the weld pool in GTA welding. Especially, the differences between the welding of a low sulfur stainless steel and of a high sulfur stainless steel are focused.

2. Simulation Model

This model is concerned with the stationary GTA welding using a tungsten cathode of 3.2 mm diameter with a 60 degrees conical tip. Fig. 1 shows the calculation domain described in the two-dimensional cylindrical coordinate assuming rotational symmetry around the arc axis. The anode is a low sulfur stainless steel which contains 10 ppm sulfur or a high sulfur stainless steel which contains 220 ppm sulfur. The anode temperature is initially set to be 300 K and the melting points of both stainless steels are 1750 K. Helium shielding gas is supplied from the outside of the cathode on the upper boundary at the flow rate of 30 L/min.

The governing equations used in the model are shown as follows:

The mass continuity equation is,

$$\frac{\partial \rho}{\partial t} + \frac{1}{r}\frac{\partial}{\partial r}(r\rho v_r) + \frac{\partial}{\partial z}(\partial v_z) = 0 \tag{1}$$

The radial momentum conservation equation is,

$$\frac{\partial \rho v_r}{\partial t} + \frac{1}{r}\frac{\partial}{\partial r}(r\partial v_r^2) + \frac{\partial}{\partial z}(\rho v_z v_r) = -\frac{\partial p}{\partial r} - j_z B_\theta + \frac{1}{r}\frac{\partial}{\partial r}\left(2r\eta\frac{\partial v_r}{\partial r}\right) + \frac{\partial}{\partial z}\left(\eta\frac{\partial v_r}{\partial z} + \eta\frac{\partial v_z}{\partial r}\right) - 2\eta\frac{v_r}{r^2} \tag{2}$$

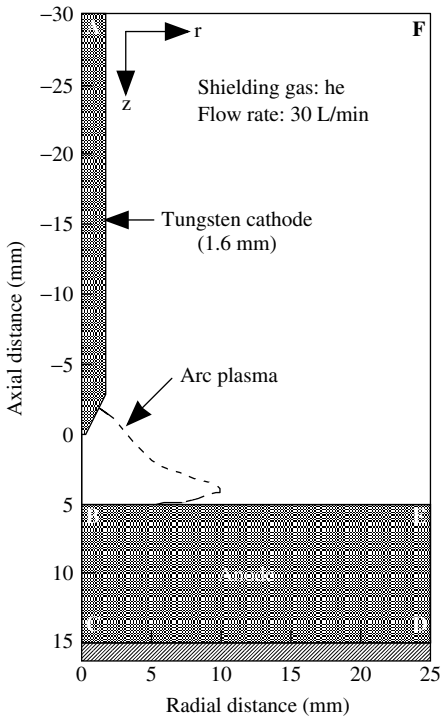

Fig. 1 Schematic illustration of simulation domain

The axial momentum conservation equation is

$$\frac{\partial \rho v_z}{\partial t} + \frac{1}{r}\frac{\partial}{\partial r}(r\rho v_r v_z) + \frac{\partial}{\partial z}(\rho v_z^2) = -\frac{\partial p}{\partial z} - j_r B_\theta + \frac{\partial}{\partial z}\left(2\eta\frac{\partial v_z}{\partial r}\right) + \frac{1}{r}\frac{\partial}{\partial r}\left(r\eta\frac{\partial v_r}{\partial z} + r\eta\frac{\partial v_z}{\partial r}\right) + \rho g \tag{3}$$

The energy conservation equation is,

$$\frac{\partial \rho h}{\partial t} + \frac{1}{r}\frac{\partial}{\partial r}(r\rho v_r h) + \frac{\partial}{\partial z}(\rho v_z h) = \frac{1}{r}\frac{\partial}{\partial r}\left(\frac{r\kappa}{c_p}\frac{\partial h}{\partial r}\right) + \frac{\partial}{\partial z}\left(\frac{\kappa}{c_p}\frac{\partial h}{\partial r}\right) + j_r E_r + j_z E_z - U \tag{4}$$

The current continuity equation is,

$$\frac{1}{r}\frac{\partial}{\partial r}(r j_r) + \frac{\partial}{\partial z}(j_z) = 0 \tag{5}$$

$$j_r = -\sigma E_r,\ j_z = -\sigma E_z \tag{6}$$

where t is time, h is enthalpy, p is pressure, v_r and v_z are radial and axial velocities, j_r and j_z are the radial and axial components of the current density, g is acceleration due to gravity, c_p is specific heat, κ is thermal conductivity, ρ is density, η is viscosity, and σ is electrical conductivity. U is radiative emission coefficient and absorption is not considered. E_r and E_z are the radial and axial components of the electric field defined by:

$$E_r = -\frac{\partial V}{\partial r}, \quad E_z = -\frac{\partial V}{\partial z} \tag{7}$$

where, V is electric potential. The temperature at boundaries CD, DE, EF, and FA in Fig. 1 are set to be 300 K. In the tungsten cathode and the solid anode where the temperature is less than the melting point, v_r and v_z are set to be zero. Furthermore, v_z is set to be zero at the anode surface BE in Fig. 1. The azimuthal magnetic field, B_θ induced by arc current is evaluated by Maxwell's equation:

$$\frac{1}{r}\frac{\partial}{\partial r}(r B_\theta) = \mu_0 j_z \tag{8}$$

where, μ_0 is the permeability of free space. It is necessary to consider the effects of energy transfer at the electrode surfaces. The additional energy fluxes at the cathode and anode are described as:

$$\text{Cathode: } F_K = -\varepsilon\alpha T^4 - |j_e|\phi_K + |j_i|V_i \tag{9}$$

$$\text{Anode: } F_A = -\varepsilon\alpha T^4 - |j|\phi_A \tag{10}$$

where, ε is surface emissivity, α is the Stefan-Boltzmann constant, ϕ_K is the work function of the tungsten cathode, V_i is the ionization potential of the plasma gas, j_e is the electron current density, j_i is the ion current density, φ_A is the work function of the anode and T is the temperature. For the cathode surface, F_K needs to be included in Equation (4) to take into account the thermionic cooling by emission of electrons, radiative cooling and ion heating. Similarly, for the anode surface, F_A is required in Equation (4) to take into account radiative cooling and thermionic heating. Furthermore, for the cathode surface, the electron current and the ion current are

considered separately and defined based on the Richardson-Dushman equation of thermionic emission as follows:

$$j_R = AT^2 \exp\left(-\frac{e\phi_K}{k_B T}\right) \tag{11}$$

where, k_B is the Boltzmann's constant and A is the Richardson's constant, which depend on the cathode material. The ion current density, j_i is then assumed to be, where the total current density, j is $|j| = |j_e| + |j_i|$.

The convection in the weld pool is influenced by the shear stress caused by the convective flow of the cathode jet, the Marangoni force induced by the gradient in the surface tension of the weld pool, the buoyancy due to gravity and the electromagnetic pinch force due to the arc current. If only the driving forces of the weld pool convection at the boundary between the weld pool and the arc plasma are considered, the shear stress caused by the plasma flow is already included in η in Equation (2). Therefore, only the Marangoni force is added, which is given by [4]:

$$M_A = \frac{\partial}{\partial z}\left(\frac{\partial \gamma}{\partial T}\frac{\partial T}{\partial r}\right) \tag{12}$$

where, γ is the surface tension of the weld pool. It is assumed in this study that the stainless steel contains 10 ppm or 220 ppm sulfur. In case of 10 ppm sulfur, the variation of the surface tension at the weld pool surface decrease linearly with increasing temperature ($\partial\gamma\partial T = -4.6 \times 10^{-4}$ N/mK) [4], while in case of 220 ppm sulfur, the variation of the surface tension increase linearly with increasing temperature ($\partial\gamma\partial T = 2.1 \times 10^{-4}$ N/mK).

A mass conservation equation expressed by Equation (13) is applied to take a metal vapor behavior into account [7]. As metal vapor in an arc plasma, Fe, Cr, Ni, and Mn [8] are considered because stainless steel is used. However, only iron vapor is take into account in this study to simplify the model and facilitate calculation.

$$\frac{\partial}{\partial t}(\rho C_1) + \frac{1}{r}\frac{\partial}{\partial r}(r\rho v_r C_1) + \frac{\partial}{\partial z}(\rho v_z C_1) = \frac{1}{r}\frac{\partial}{\partial r}\left(r\rho D\frac{\partial C_1}{\partial r}\right) + \frac{\partial}{\partial z}\left(\rho D\frac{\partial C_1}{\partial z}\right) \tag{13}$$

where, C_1 is mass fraction concentration of iron vapor and D is the two-dimensional diffusion coefficient which is expressed by the viscosity approximation equation:

$$D = \frac{2\sqrt{2}\,(1/M_1 + 1/M_2)^{0.5}}{\left\{\left(\rho_1^2/\beta_1^2\eta_1^2 M_1\right)^{0.25} + \left(\rho_2^2/\beta_2^2\eta_2^2 M_2\right)^{0.25}\right\}^2} \tag{14}$$

where, M_1 and M_2 are the molecular weights of iron and the shielding gas, respectively. ρ_1, ρ_2, η_1 and η_2 are the density and viscosity of iron and helium gas, respectively. β_1, β_2 are the dimensionless constants, and theoretically range between 1.2 and 1.543 for various kinds of gas such as Ar, He, H_2, N_2, O_2 and CO_2. $\beta_1 = \beta_2$ 1.385 is assumed based on the mean value of the experimental data [9]. The viscosity approximation is not strictly justified since it does not take ionized matters into account. However, it is relatively accurate up to 30 000 K [10] and considered to be suitable for modeling welding arcs.

C_1 is set to be zero in the cathode area and in the anode area. However, at the anode surface where the temperature is above the melting point, C_1 is given as [7]:

$$C_1 = \frac{p_{v,1} M_1}{p_{v,1} M_1 + \left(p_{atm} - p_{v,1}\right) M_2} \tag{15}$$

where, p_{atm} is the atmospheric pressure, and $p_{v,1}$ is the iron vapor partial pressure which is a function of the weld pool temperature [11]. According to Equation (15), C_1 varies between zero and 1.0. For the other boundary conditions, $C_1 = 0$ at AF and FE shown in Fig. 1, and $\partial C_1/\partial r = 0$ at the arc axis (AB). Entering iron vapor into the arc plasma should be given as a source term to Equation (1). However, it is considered that iron vapor replace helium gas in this model.

Plasma properties, such as enthalpy, electrical conductivity, specific heat, thermal conductivity, density, viscosity and radiative emission coefficient, are dependent on not only the temperature but also the mole fraction of iron vapor. The plasma properties at the intermediate concentrations of iron vapor are calculated using a linear approximation based on the properties at 0, 1, 10 and 20 mol% of iron vapor mixture rate. The properties were calculated using the Chapman-Enskog approximation [12] under the assumption that the arc plasma is in a local thermodynamic equilibrium (LTE) condition. For example, the electrical conductivities [13], which are significantly affected by the mixture of iron vapor, are shown in Fig. 2. The electrical conductivity of iron vapor is also shown for reference. Concerning the change in electrical conductivity of helium plasma, electrical conductivity greatly increases by the addition of iron vapor at temperatures below 15 000 K, and the effect of the iron vapor addition does not differ between 10 and 20 % of the mixing ratio.

The governing and auxiliary equations were solved iteratively by the SIMPLEC numerical procedure. The other approximations and boundary conditions are given in the present authors' previous papers [5,14].

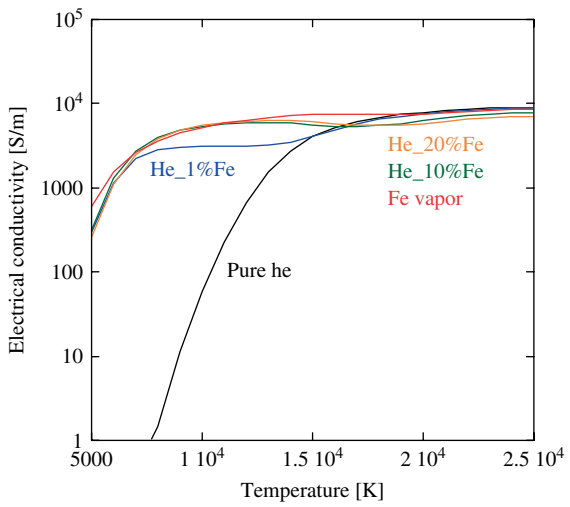

Fig. 2 Dependence of electrical conductivities of helium gas on temperature for each mixing ratio

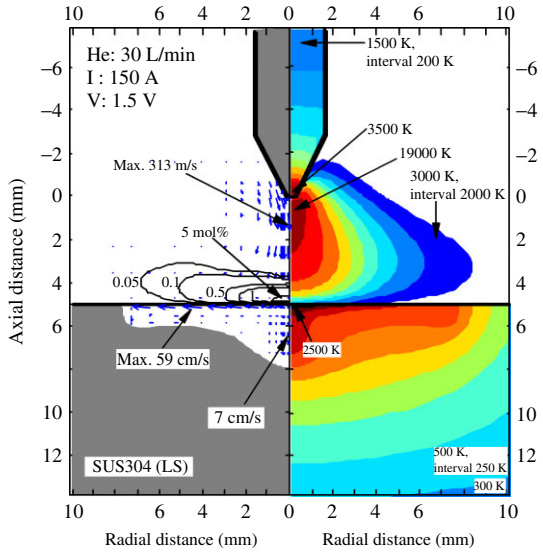

Fig. 3 Calculated results for helium GTA welding of a low sulfur stainless steel at 20 s after arc ignition

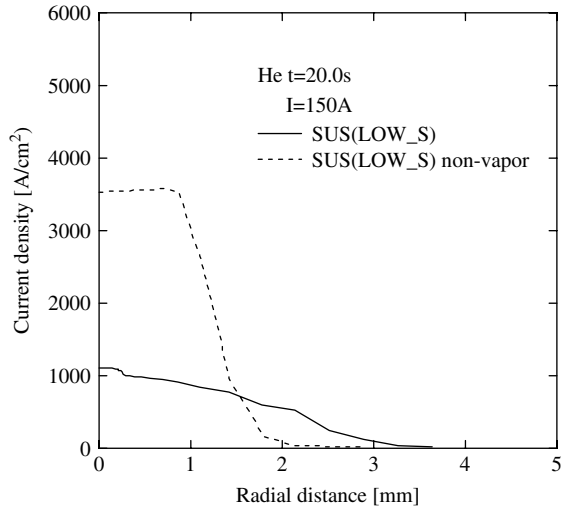

Fig. 4 Radial distributions of the current density on the low sulfur stainless steel anode

3. Results

The present model was applied to the case of stationary helium GTA welding of stainless steel. Fig. 3 shows the two-dimensional distribution of the temperature, weld penetration, fluid flow velocity and mole fraction of iron vapor at 20.0 s after arc ignition for a low sulfur stainless steel. The weld pool mainly grows in the radial direction because of the Marangoni force and shear stress caused by the convective flow of the cathode jet. The distribution of iron vapor is determined by the diffusion term and the convection term as described in Equation (13). In an arc atmosphere where high-speed plasma flow of 300 m/s exists, the convection term dominates. It is thus seen that distribution of iron vapor expands in the radial direction, concentrating just above the weld pool surface. The concentration of iron vapor mixed in arc plasma attains to 7 mol%. This result is in good agreement with the experimental data by Terasaki [8].

Figure 4 shows the radial distributions of current density on the low sulfur stainless steel anode. The distribution calculated neglecting the effect of iron vapor on the arc plasma is also shown to demonstrate the influence of iron vapor. The current density distribution obviously differs. The peak current density when iron vapor is neglected is over 3500 A/cm^2, while that decreases to 1100 A/cm^2 under the existence of iron vapor. The current path is expanded by the increase of the electric conductivity at lower temperatures as shown in Fig. 2.

Fig. 5 shows the two-dimensional distribution of the temperature, weld penetration, fluid flow velocity and mole fraction of iron vapor at 20 s after arc ignition for a high sulfur stainless steel. Temperature of arc plasma is almost same to that for a low sulfur stainless steel. However, the weld pool shape shows much deeper penetration. This is because marangoni force works in the reverse direction due to the effect of sulfur. Upward flow occurs just above the weld pool surface, which is not seen in the calculation of a low sulfur stainless steel. Therefore, the distribution of iron vapor expands higher than

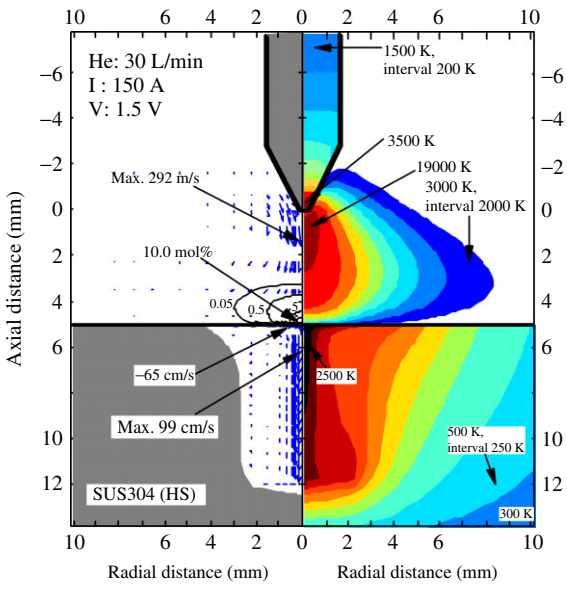

Fig. 5 Calculated results for helium GTA welding of a high sulfur stainless steel at 20 s after arc ignition

that for a low sulfur stainless steel, and does not expand in the radial direction.

Figures 6 and 7 show the cross sections of the weld bead in the calculation and experiment for a low sulfur stainless steel and a high sulfur stainless steel, respectively. The experiment is consistent with the calculation. The work piece is SUS304 stainless plate (50 × 100 × 10 mm thick) with 10 ppm sulfur, or 220 ppm sulfur content, mounted on a water-cooled copper plate. The welding conditions, such as arc length, electrode diameter and flow rate of shielding gas, are the same as the conditions of the calculation. Both calculation results show good agreement with the experimental results.

Figure 8 shows the radial distributions of iron vapor concentration above the anode. The iron vapor for a low sulfur

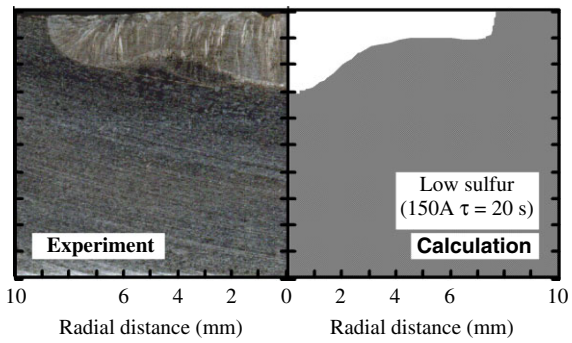

Fig. 6 Cross-section of welding bead of a low sulfur stainless steeel

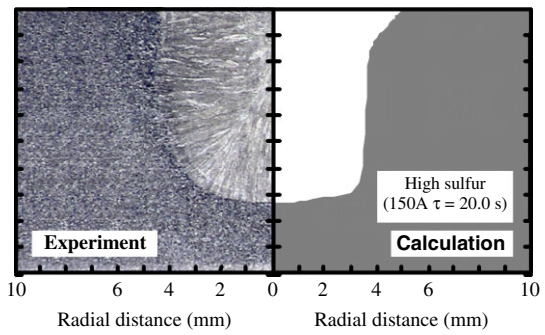

Fig. 7 Cross-section of the welding bead of a high sulfur stainless steel

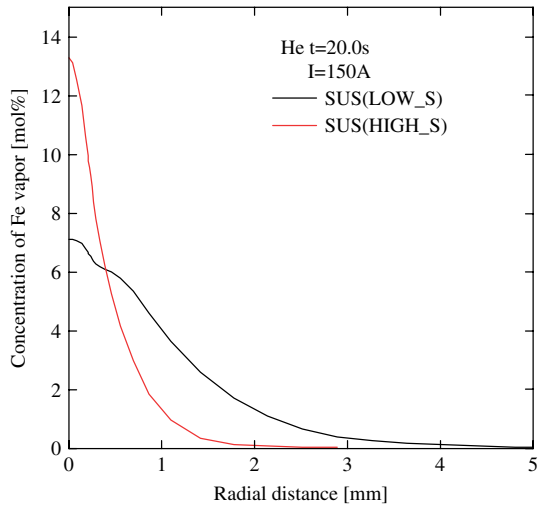

Fig. 8 Radial distributions of the iron vapor concentration above the anode

stainless steel expands widely. The iron vapor for high sulfur stainless steel is concentrated around the arc axis and drastically decreases with being away from the arc axis.

Figure 9 shows the radial distributions of current density on the low sulfur stainless steel anode and on the high sulfur stainless steel anode. The current path shows the same tendency of the distribution of iron vapor though it is less remarkable.

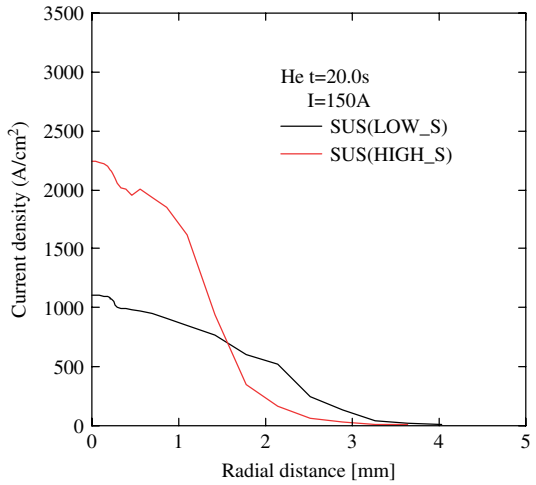

Fig. 9 Radial distributions of the current density on the low sulfur stainless steel anode and on the high sulfur stainless steel anode

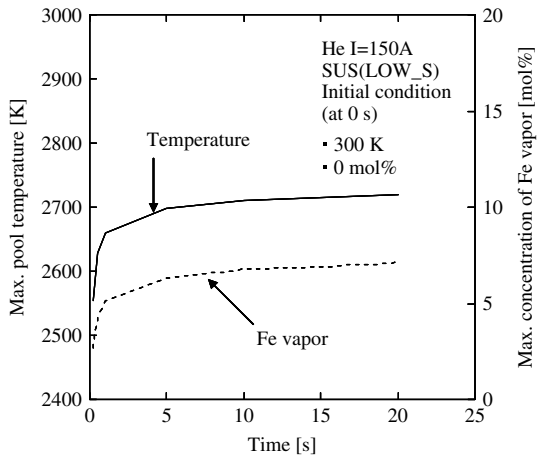

Fig. 10 Relation between maximum weld pool temperature and maximum concentration of iron vapor in the welding of a low sulfur stainless steel

Figures 10 and 11 show the calculation results of transient maximum concentration of iron vapor in arc plasma and transient maximum temperature of the weld pool for a low sulfur stainless steel and a high sulfur stainless steel (at 0.2, 0.5, 1.0, 5.0, 10.0 and 20.0 s after arc ignition), respectively. The iron vapor concentration increases with increasing weld pool temperature for a low sulfur stainless steel. However, the maximum iron vapor concentration is highest after arc ignition for high sulfur stainless steel, and then decreases with decreasing weld pool temperature. This difference is caused by the direction of the convection in the weld pool. In the case of a low sulfur stainless steel anode, due to the convection toward the outside of the weld pool, the heat expands widely. Therefore, weld pool temperature gradually increases. In the case of a high sulfur stainless steel anode, due to the convection toward the inside of the weld pool surface, the heat concentrates at the center area. Therefore, the weld pool becomes locally significant high temperature. Then, the concentration of heat

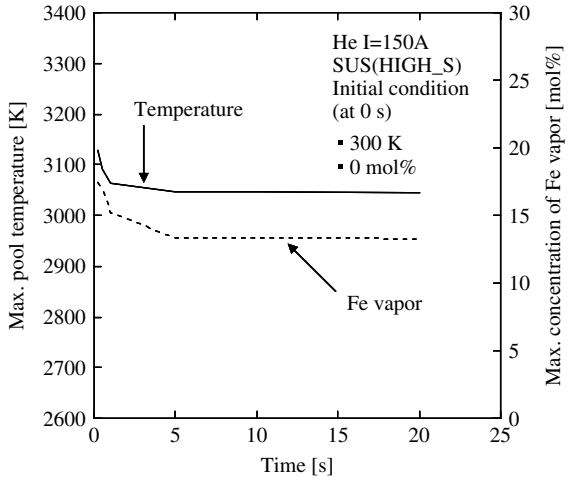

Fig. 11 Relation between maximum weld pool temperature and maximum concentration of iron vapor in the welding of a high sulfur stainless steel

is eased as the weld pool grows, and maximum temperature decreases.

4. Conclusions

A numerical model of the stationary GTA welding taking into account iron vapor from the weld pool surface is developed and the effect of iron vapor on the properties of the arc and weld pool are simulated. The main conclusions are summarized as follows:

(1) In the calculation for the welding of a low sulfur stainless steel, iron vapor expands in the radial direction and concentrates just above the weld pool surface beneath the arc. In case of a high sulfur stainless steel, upward flow from the anode occurs, therefore, iron vapor expands higher than that in case of a low sulfur stainless steel.
(2) In the case of a low sulfur stainless steel, the radial distribution of current density on the anode expands more widely than that of a high sulfur stainless steel due to the increase of electrical conductivity which is caused by the inclusion of iron vapor into arc plasma.
(3) The maximum iron vapor concentration increases with increasing weld pool temperature after arc ignition for a low sulfur stainless steel. However, in case of high sulfur stainless steel, the maximum iron vapor concentration is highest at arc ignition, and then decreases with decreasing weld pool temperature.

References

(1) Tanaka M, Watanabe T, Isa T, Nishiwaki H. New development of welding and thermal spraying. *J. Plasma & Fusion Res.* 2006; **82(8)**:492–496, (in Japanese).
(2) Fan HG, Kovacevic R. The front line of modeling heat and mass transfer in arc welding processes. *J. Japan Welding Soc.* 2007; **76(2)**:82–89.
(3) Nishiyama H, Sawada T, Takana H, Tanaka M, Ushio M. Computational simulation of arc melting process with complex interactions. *ISIJ Int.* 2006; **46(5)**:705–711.
(4) Tanaka M, Lowke JJ. Predictions of weld pool profiles using plasma physics. *J. Phys. D* 2007; **40**:R1–R23.
(5) Tashiro S, Tanaka M, Nakata K, Iwao T, Koshiishi F, Suzuki K, Yamazaki K. Plasma properties of helium gas tungsten arc with metal vapor. *Sci. Technol. Weld. Join.* 2007; **12(3)**:202–207.
(6) Fan HG, Kovacevic R. A unified model of transport phenomena in gas metal arc welding including electrode, arc plasma and molten pool. *J. Phys. D* 2004; **37**:2531–2544.
(7) Menart J, Lin L. Numerical study of a free-burning argon arc with copper contamination from the anode. *Plasma Chem. & Plasma Process.* 1999; **19(2)**:153–170.
(8) Terasaki H, Tanaka M, Ushio M. Effects of metal vapor on plasma state in helium gas tungsten arcs. *Quarterly J. Japan Welding Soc.* 2002; **20(2)**:201–206.
(9) Wilke CR. A viscosity equation for gas mixtures. *J. Chem. Phys.* 1950; **18(4)**:517–519.
(10) Murphy AB. A comparison of treatments of diffusion in thermal plasmas. *J. Phys. D* 1996; **29**:1922–1932.
(11) The Japan Institute of Metals: *Edition No. 3 Data Book of Metals*, Tokyo, Maruzen Co., Ltd, 86–92 1993; (in Japanese).
(12) Murphy AB. Transport Coefficients of Air, Argon-Air, Nitrogen-Air, and Oxygen-Air. *Plasma Chem. Plasma Process.* 1995; **15(2)**:279–307.
(13) Boulos MI, Fauchais P, Pfender E. *THERMAL PLASMAS*. Plenum Press: New York; 1994,; 135–139.
(14) Tashiro S, Tanaka M, Nakatani M, Furubayashi M, Yamazaki Y. Properties of Mass and Heat Transfer for Tube Cathode Arcs. *Quarterly J. Japan Welding Soc.* 2007; **25(1)**:3–9, (in Japanese).

Kentaro Yamamoto (Non-member) was born in Osaka Prefecture, Japan, in 1981. He received the B.Eng. degree and the M.Eng. degree from Osaka University, Osaka, Japan, in 2005 and 2007, respectively. His research interests are numerical simulations of arc welding.

Manabu Tanaka (Member) was born in Wakayama Prefecture, Japan, in 1967. He received the B.Eng. degree, the M.Eng. degree in welding, and the Ph.D. degree from Osaka University, Osaka, Japan, in 1990, 1992, and 2000, respectively. In 1992, he became a Research Associate with the Joining and Welding Research Institute, Osaka University. In 2000, he was a Visiting Scientist at the CSIRO Telecommunications and Industrial Physics, Lindfield, Australia. He became an Associate Professor in 2003 and a Professor in 2008, with the Joining and Welding Research Institute, Osaka University. His research interests include the physics of welding, including plasma diagnostics, electrode phenomena, and numerical modeling.

Shinichi Tashiro (Member) received his D.Eng. degree in electrical engineering from Chuo University in 2005. He is now an assistant professor at Osaka University. His research interests are physics of welding, atmospheric discharge and numerical simulation.

Kazuhiro Nakata (Non-member) was born in 1949. He received the B.Eng. degree, the M.Eng. degree in welding, and the Ph.D. degree from Osaka University, Osaka, Japan, in 1972, 1974, and 1993, respectively. In 1977, he became a Research Associate with the Joining and Welding Research Institute, Osaka University. He became an Associate Professor in 1994, and a Professor in 2002 with the Joining and Welding Research Institute, Osaka University. His research interests are Friction Stir Welding, surface modification of material.

Anthony B. Murphy (Non-member) was born in Sydney, Australia, in 1960. He received the B.Sc. (honors) and Ph.D. degrees from the University of Sydney in 1981 and 1987, respectively. From 1987 to 1989, he was a Postdoctoral Scientist at the Max-Planck-Institut for Plasma physics, Munich, Germany, in the field of radio-frequency heating of fusion plasmas. Since 1989, he has been with Commonwealth Scientific and Industrial Research Organisation (CSIRO) Telecommunications and Industrial Physics, Sydney, where he is a Senior Principal Research Scientist. His research interests include transport properties and modeling of thermal plasmas, plasma waste destruction, and corona discharges.